UC Berkeley
UC Berkeley Previously Published Works

Title

Production of C2/C3 Oxygenates from Planar Copper Nitride-Derived Mesoporous Copper via Electrochemical Reduction of CO2

Permalink

https://escholarship.org/uc/item/9jv1p554

Journal

Chemistry of Materials, 32(7)

ISSN

0897-4756

Authors

Ebaid, Mohamed
Jiang, Kun
Zhang, Zemin
et al.

Publication Date

2020-04-14

DOI

10.1021/acs.chemmater.0c00761

Peer reviewed

Production of C₂/C₃ Oxygenates from Planar Copper Nitride-Derived Mesoporous Copper via Electrochemical Reduction of CO₂

Mohamed Ebaid[†,◻], Kun Jiang[†,§,¥,◻], Zemin Zhang[†], Walter S. Drisdell[†,‡], Alexis T. Bell[†,§,*], and Jason K. Cooper[†,‡,*]

[†]Joint Center for Artificial Photosynthesis, Lawrence Berkeley National Laboratory, Berkeley, California 94720, USA
[‡]Chemical Sciences Division, Lawrence Berkeley National Laboratory, Berkeley, California 94720, USA
[§]Department of Chemical and Biomolecular Engineering, University of California, Berkeley, California 94720, USA
[¥] School of Mechanical Engineering, Shanghai Jiao Tong University, Shanghai 200240, China

[◻]Contributed equally

[*]E-mail: jkcooper@lbl.gov and alexbell@berkeley.edu

ABSTRACT

Electrochemical reduction of CO_2 provides an opportunity to produce fuels and chemicals in a carbon-neutral manner, assuming that CO_2 can be captured from the atmosphere. To do so, requires efficient, selective, and stable catalysts. In this study, we report a highly mesoporous metallic Cu catalyst prepared by electrochemical reduction of thermally nitrided Cu foil. Under aqueous saturated CO_2 reduction conditions, the Cu_3N-derived Cu electrocatalyst produces virtually no CH_4, very little CO, and exhibits a Faradaic efficiency of 68% to C_{2+} products (C_2H_4, C_2H_5OH, and C_3H_7OH) at a current density of ~18.5 mA cm^{-2} and a cathode potential of -1.0 V vs. the reversible hydrogen electrode (RHE). Under these conditions, the catalyst produces more oxygenated products than hydrocarbons. We show that surface roughness is a good descriptor of catalytic performance. The roughest surface reached 98% CO utilization efficiency for C_{2+} product formation from CO_2 reduction and the ratio of oxygenated to hydrocarbon products correlates with the degree of surface roughness. These effects of surface roughness are attributed to the high population of under-coordinated sites as well as a high pH environment within the mesopores and adjacent to the surface of the catalyst.

INTRODUCTION

Anthropogenic emissions of greenhouse gases are responsible for the increase in global mean temperature, which is threatening the Earth's ecosystem and its inhabitants.[1, 2] Therefore, there is a strong interest in exploring strategies for using atmospheric CO_2 as a renewable source of carbon to produce transportation fuels and chemicals. A possible route towards achieving this goal is electrochemical reduction of CO_2. Successful development of this concept into a technology requires the discovery and development of energy-efficient, stable, and selective catalysts for producing hydrocarbons and alcohols. Though various transition metals,[3] metal alloys,[4] and chalcogenides[5, 6] have been reported to promote the electrochemical CO_2 reduction reaction (CO_2RR), Cu remains the only electrocatalyst capable of generating multi-carbon products from CO_2/CO with high Faradaic efficiency (FE).[7-14]

Different strategies have been explored to improve the selectivity towards multi-carbon products on Cu. Roughening Cu surfaces by the *in-situ* reduction of Cu_2O[10, 11, 15] or Cu_3N[16] during CO_2 reduction has been found to be the most efficient way to achieve a high selectivity C_{2+} products in aqueous electrolytes. Such modified Cu surfaces have been reported to generate catalytically active sites by the creation of intrinsic defects such as grain boundaries, stepped sites, and other surface defects, which can bind CO and other intermediates strongly and promote C-C bond formation.[17, 18] Other factors such as local pH,[19] temporal intermediates trapping by nano-/meso-cavities[20,21] and cation-induced electric fields[22] have also been found to enhance the formation of multi-carbon products. The relatively low selectivity to products involving more than two carbon atoms, in particular C_3 products (allyl alcohol and n-propanol), also remains an issue for virtually all Cu-based catalysts.[16, 23-25] Although surface roughening has contributed to the selective formation of multi-carbon products on Cu, there remains a need for novel ways to produce Cu surfaces with a more controlled roughness in order

to clearly investigate the structure-activity relationship of CO_2RR performances.

Herein we report a novel method to produce highly roughened mesoporous Cu catalyst that significantly differs from the single crystalline Cu electrodes produced by Bridgeman method[10] or metal ion battery cycling[11] as well as the electrochemically deposited Cu_2O oriented films on Cu substrates[15]. This mesoporous Cu catalyst delivers state-of-the-art performance for aqueous CO_2RR. At -1.0 V vs. the reversible hydrogen electrode (RHE), the Faradaic efficiency to multi-carbon products (C_{2+}) exceeds 68%, and ~35% of this amount is in the form of C_{2+} oxygenates of which ~10% is n-propanol (C_3). Only 1.1% CO and no detectable methane are formed at a current density of ~18.5 $mA.cm^{-2}$. Uniform Cu_3N films are produced by thermal nitriding of Cu foil at atmospheric pressure in a stream of NH_3/O_2. These materials are characterized *in-situ* by X-ray diffraction (XRD) and *ex-situ* by high-resolution scanning transmission electron microscopy (HR-STEM), X-ray absorption spectroscopy (XAS), and X-ray photoelectron spectroscopy (XPS). Under CO_2RR conditions, the Cu_3N precursor is reduced to a highly porous metallic Cu structure, exhibiting an electrochemical surface roughness > 17 compared to an electro-polished Cu foil. The outstanding CO_2RR performance of such Cu_3N-derived Cu is attributed to a high population of under-coordinated Cu sites as well as an increase in surface pH from local reaction environment.

EXPERIMENTAL SECTION

Cu_3N CVD fabrication. Polycrystalline Cu foils (Alfa Aesar; 0.1 mm thick, Puratronic, 99.999% metals basis) were first rinsed with Milli-Q water, dried with nitrogen, and then electrochemically polished in phosphoric acid (85% in water) by applying +2.1 V versus a graphite rod for 5 min. For the synthesis of the Cu_3N layer, the pre-cleaned Cu foil was loaded into a horizontal quartz tube reactor and heated by a two-zone Mellen furnace equipped with clamshell heating elements. Quartz tube and gas lines were

carefully evacuated prior to the introduction of the reactive gases. The Cu foil was then annealed at 550 °C in an NH_3/O_2 mixture for a period of 15 to 60 min at atmospheric pressure. The flows of NH_3 and O_2 were introduced through calibrated mass flow controllers in order to achieve a total flow rate of 75 sccm, with a nominal concentration of 2 vol% O_2. The annealed Cu foils were slowly cooled down to room temperature under the same gas environment before they were taken out of the reactor.

Physical characterization. *In-situ* XRD diffraction patterns were obtained using a Rigaku Smartlab X-ray diffractometer equipped with a ReactorX attachment; a corrosion resistant high-temperature reactor, and a HyPix-3000 high-energy-resolution 2D multidimensional semiconductor detector. The incident X-ray beam was filtered using a double-crystal high-resolution PB-Ge (220)x2 monochromator. The surface morphology was visualized using SEM (Quanta FEG 250, FEI). The microstructures were investigated by cross-sectional HAADF-STEM using a probe-corrected FEI Titan Themis 300 S/TEM with ChemiSTEM technology operated at 300 kV. TEM sample preparation was performed using the standard lift-out procedure with an FEI Scios Dual-Beam focused ion beam (FIB)-SEM system. EDS analysis was performed at 300kv using a Super-X EDS system. The surface compositions were investigated using XPS acquired by a Kratos Axis Ultra spectrometer using an Al Kα source (hν = 1486.69 eV) operated at 225 W and a hemispherical electron energy analyzer. XPS binding energies were calibrated using adventitious alkyl carbon signals by shifting the C 1s peak to 284.8 eV. The XAS data were acquired at beamline 9-3 (BL9-3) at Stanford Synchrotron Radiation Lightsource (SSRL), SLAC National Accelerator Laboratory. The SPEAR3 storage ring operated at 500 mA and 3.0 GeV. BL9-3 is equipped with a rhodium-coated vertical collimating mirror upstream of the Si(220) monochromator and an additional downstream rhodium-coated bent-cylindrical focusing mirror. Harmonic rejection was accomplished by setting the cut-off angle of the mirrors to an appropriate energy. Incident and transmitted X-rays were monitored using gas ionization chambers and X-ray

5

absorption was measured as the primary fluorescence excitation spectrum using an array of 100-element Ge detector.

Electrochemical measurements. All electrochemical experiments were conducted in a gas-tight electrochemical cell machined from polyether ether ketone (PEEK).[27] A graphite rod (99.995%, Sigma Aldrich) was used as the counter electrode, placed parallel to the working electrode and separated by an anion conducting membrane (Selemion AMV AGC Inc.). Gas dispersion frits were incorporated into both electrode chambers to provide ample electrolyte mixing. The exposed geometric surface area of each electrode was 1 cm^2 and the electrolyte volume of each electrode chamber was 1.8 cm^3. A leak-free Ag/AgCl electrode (Innovative Instruments Inc.) was used as the reference electrode, all potentials were measured against Ag/AgCl and then converted to the RHE scale using the relationship E (vs RHE) = E (vs Ag/AgCl) + 0.197 V + 0.0591×pH, where pH values of electrolytes were determined by an Orion Dual Star Benchtop Meter (Thermo Scientific). A 0.05 M M_2CO_3 (99.995%, Sigma Aldrich) solution prepared using Milli-Q water was used as the electrolyte. Metallic impurities in the as-prepared electrolyte were removed before electrolysis by chelating the solution with Chelex 100 (Na form, Sigma Aldrich). Both electrode chambers were sparged with CO_2 (99.999%, Praxair Inc.) at a rate of 20 sccm for 40 min prior to and throughout CO_2 electrolysis. Prior to CO_2RR measurements, a pre-reduction step was carried out for 90 min chronoamperometry at -0.6 V in CO_2-saturated 0.1 M $CsHCO_3$. Electrochemistry was performed with a Biologic VSP-300 potentiostat. Potentiostatic electrochemical impedance spectroscopy (PEIS) and current interrupt (CI) methods were used to determine the uncompensated resistance (R_u) of the electrochemical cell. The potentiostat compensated for 85% of R_u *in situ*. The roughness factors of Cu foil electrodes were determined relative to the electrochemically polished one, by taking the ratio of their double layer capacitances measured after 1-h electrolysis.

CO₂RR products quantification. The effluent from the electrochemical cell was analyzed using an Agilent 7890B gas chromatograph (GC) equipped with a pulsed-discharge helium ionization detector (PDHID). He (99.9999%, Praxair Inc.) was used as the carrier gas. The constituents of the gaseous sample were separated using a Hayesep-Q capillary column (Agilent) connected in series with a packed ShinCarbon ST column (Restek Co.). The signal response of the PDHID was calibrated by analyzing a series of NIST-traceable standard gas mixtures (Airgas Inc.). The partial current density for a given gas product was calculated as $j_i = x_i \times v \times \dfrac{n_i F p_0}{RT} \times (electrode\,area)^{-1}$, where x_i is the volume fraction of certain product determined by online GC, v is the flow rate, n_i is the number of electrons required to form product i, $p_0 = 101.3$ kPa, F is the Faradaic constant and R is the gas constant. The corresponding FE at each potential is calculated using the relationship $FE = j_i / i_{total} \times 100\%$. The electrolyte from cathodic chamber was collected after electrolysis and analyzed using a Thermo Scientific UltiMate 3000 liquid chromatography (HPLC) equipped with a refractive index detector (RID). The electrolyte samples were stored in a refrigerated autosampler at 10 °C before analysis to minimize the evaporation of volatile products. The liquid-phase products contained in a 20 μL aliquot were separated using two Aminex HPX 87-H columns (Bio-Rad Inc.) connected in series and a 1 mM sulfuric acid eluent (99.999%, Sigma Aldrich). The column oven was maintained at 60 °C for the duration of the analysis. The signal response of the RID was calibrated by analyzing standard solutions of each product at a concentration of 1, 10, and 50 mM.

RESULTS AND DISCUSSION

Cu_3N was prepared by thermal annealing of an electropolished Cu foil at atmospheric pressure in a NH_3/O_2 mixture for 15 to 60 min at a temperature of 550°C which resulted in formation of a film of Cu_3N on the surface of the

Cu foil. The growth of Cu_3N proceeds from top to bottom. It starts with the formation of a surface copper oxide that serves to activate the dehydrogenation of NH_3 producing water and copper nitride.[26, 27,28, 29] After thermal nitriding, the resulting film has a green color and is confirmed by XRD to be Cu_3N, which has an anti-ReO_3 (anti-perovskite) cubic structure built up of eight corner-sharing NCu_6 octahedra (Figure 1A).

The relatively smooth surface of the electropolished Cu foil was significantly roughened as a result of the formation of Cu_3N, as revealed by scanning electron microscopy (SEM) (Figure 1B and 1C). This can be attributed to the crystallographic transformation of the Cu crystal lattice to accommodate the nitrogen atoms.[30] The Cu molar density is 0.141 and 0.09 mol cm^{-3} for Cu and Cu_3N, respectively. As such, a volumetric expansion of the Cu atomic density by a factor of 1.6 is necessary to accommodate the inclusion of the N atoms into the crystal. Considering the process temperature is well below the melting point of either material, the resulting film is significantly roughening by the transformation from Cu to Cu_3N. The degree of surface roughness was controlled by adjusting the nitriding time (Supporting Information, Figure S1); increasing the nitriding time increased the surface roughness.

To gain further insight into the mechanism of Cu_3N formation, the evolution of crystalline phase was monitored as a function of time and temperature by *in-situ* out-of-plane XRD using a temperature-controlled reactor (ReactorX, Rigaku-Smartlab). This leak-tight reactor enables real-time XRD measurements while keeping the sample at well-controlled temperature and in a well-controlled atmosphere. To reproduce the same conditions as those in the nitridation furnace, the same flow rates of NH_3 and O_2 but diluted by Ar (to reduce the NH_3 concentration to acceptable levels for the ReactorX) were fed to the XRD reactor through calibrated mass flow controllers. The Cu foil was heated to and maintained at 550°C for 1 h, after which it was slowly cooled down to room temperature under the same gas composition (Supporting Information, Figure S2). As shown in Figure 1D, the

formation of Cu_3N begins during heating at 400°C and is characterized by the appearance of diffraction peaks centered at 23.27° and 47.18°. These features are assigned to the (100) and (200) crystallographic planes of Cu_3N, respectively. The Cu_3N formed exhibits a preferential orientation around (100)-planes with weak contributions from (111) and (210). The underlying Cu crystal exhibits a temperature-dependent lattice constant due to thermal expansion (Supporting Information, Figure S3).[30] The crystalline quality of the Cu_3N was found to depend critically on the cooling rate. Rapid cooling led to poor Cu_3N crystallinity. These observations indicate that Cu_3N can be grown by activating NH_3 at a temperature as low as 400°C, a temperature that is much lower than that reported for similar growth techniques using nitrogen-based gas phase precursors.[27, 31] The mechanism of Cu_3N formation and growth by this technique will be discussed in a separate study.
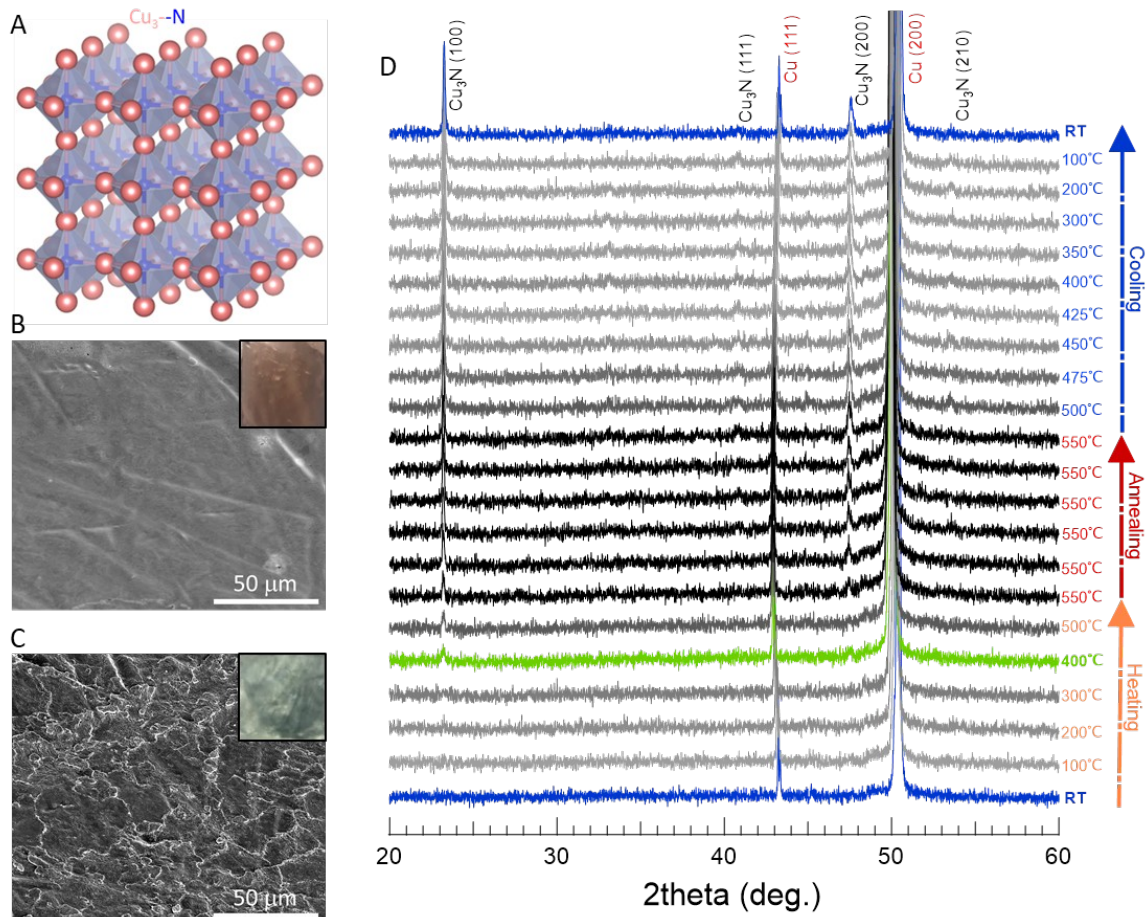
Figure 1. *In-situ* growth and surface morphology of Cu₃N. (A) Cu₃N primitive unit cell structure (space group *Pm-3m*)) with a lattice parameter of 3.81Å. Opposite to perovskites, N anion is located in Cu_3N at the octahedron center, whereas six Cu cations form a regular octahedron. Tilted-view SEM surface morphology of (B) electro-polished Cu foil and (C) Cu₃N (30 min annealing). Insets, micrographs of the Cu foil before (B) and after (C) the thermal annealing. (D) Temperature-dependent crystalline phase evolutions obtained by *in-situ* XRD.

To determine the differences in the elemental composition and the oxidation state of Cu before and after the Cu-to-Cu₃N transformation, the electronic structure of the Cu₃N was investigated by X-ray absorption near-edge structure (XANES) at the Cu K-edge. As shown in Figure 2A, the XANES spectrum of Cu₃N is distinct from that of metallic Cu due to the incorporation

of N atoms. The pre-edge peak of Cu_3N appears at 8983 eV, which is a slightly higher than the binding energy for metallic Cu. This difference is a consequence of the difference in the oxidation states of the Cu ions in Cu_3N and metallic Cu. The Cu K-edge XANES spectrum of the Cu_3N was also compared with the spectra collected for Cu_2O, CuO, and $Cu(OH)_2$ (Supporting Information, Figure S4). The absorption edge of the Cu_3N is located between those of the metallic Cu and the CuO, indicating that the oxidation state of copper ions in Cu_3N to be 1+, consistent with expectations.[32-34] The assignment of the 1+ oxidation state is also supported by XPS (Figure S5) which demonstrates no satellite peaks in the Cu 2p spectrum of the as-prepared Cu_3N.

The local coordination environment of Cu atoms in Cu_3N was also probed by extended X-ray absorption fine structure (EXAFS) at the Cu K-edge (Figure 2B). The coordination structure of Cu in Cu_3N is observed to have a strong peak due backscattering from atoms in the first coordination shell at a radial distance of 1.5 Å, in good agreement with the expected first shell scatting path of 1.45 Å. A second smaller peak at 2.1 Å was also observed. Since the expected second shell of Cu_3N is at 2.35 Å, this feature is more likely related to underlying metallic copper.[32, 35-37] The combined XAS and EXAFS results demonstrates the successful incorporation of N atoms into Cu to form Cu_3N.
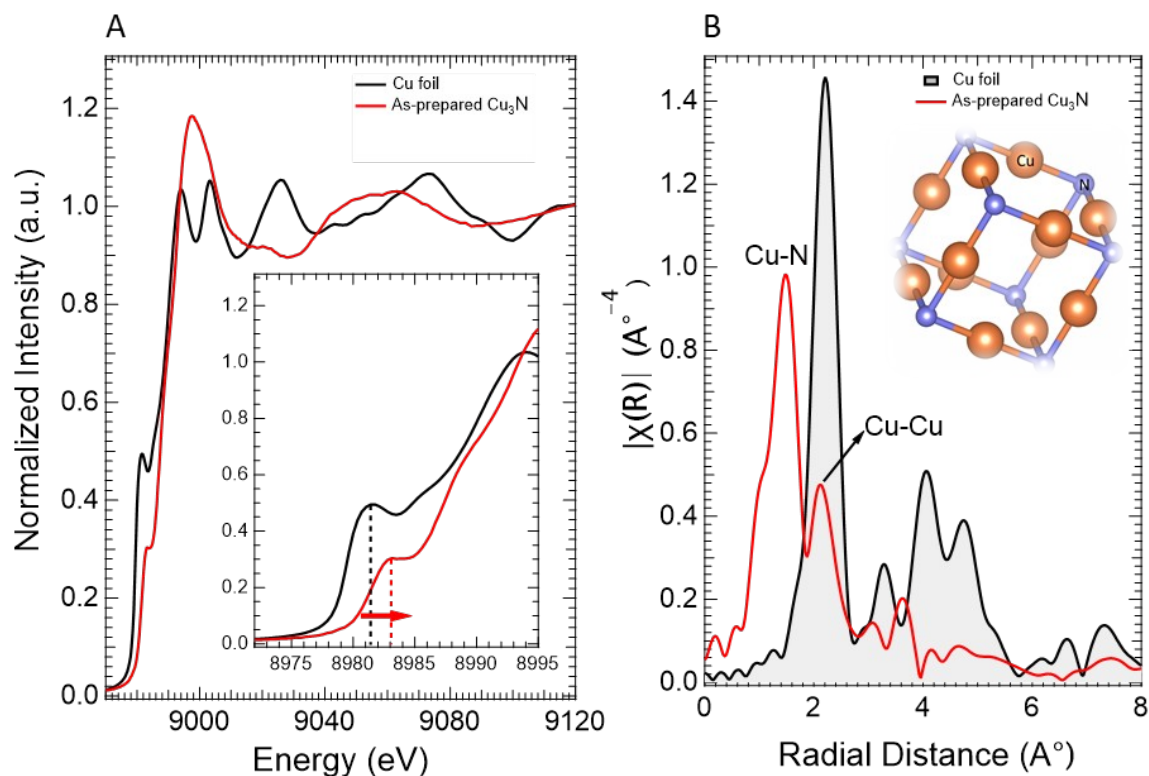
Figure 2. Fine structure and electronic states of Cu₃N. (A) Cu K-edge XANES spectra of the phase-pure Cu₃N compared to the Cu foil. Inset, a magnified view for the absorption edge shift. (B) Local coordination structure of the phase-pure Cu₃N and the Cu foil.

The nanostructure for the 30-min nitrided Cu₃N film was characterized by cross-sectional high-angle annular dark-field (HAADF)-STEM. A relatively uniform layer of Cu₃N was observed with a thickness of approximately 600 nm (Figure 3A). The formation of Cu₃N was accompanied by the appearance of a number of micro-voids at the interface between Cu₃N film and Cu foil bulk region (Supporting Information, Figure S6). The formation of these voids could be attributed to strain related defects formed during the growth of Cu₃N by the insertion of nitrogen atoms into the Cu lattice. They can also be due to oxygen impurities in the Cu foil such as native oxygen or due to the formation of surface oxide layers during thermal annealing which tend to form micro-voids at elevated temperatures.[38, 39] Both the high-resolution

transmission electron microscopy (HR-TEM) (Figure 3B) and the selective area electron diffraction (SAED) pattern (Figure 3C) are indicative of highly ordered cubic crystalline structure of phase-pure Cu_3N and the absence of any metallic Cu or Cu oxide phases within the Cu_3N layer. Elemental mapping by energy-dispersive X-ray spectroscopy (EDS) (Figure 3D) demonstrates that nitrogen is uniformly distributed within the Cu_3N film with a distinct termination at the Cu_3N/Cu foil interface (Supporting Information, Figure S7).

Prior to the electrochemical CO_2RR measurements, as-prepared Cu_3N was pre-treated by electrochemical reduction at -0.6 V vs. RHE in 0.1 M CO_2-saturated $CsHCO_3$ electrolyte for 90 min in the same manner as that done for oxide-derived Cu.[10, 11, 15] Figure S8 shows the pre-treatment current of the 30-min annealed Cu_3N. During the first 8 min a current transient was observed which amounted to 1.2 C equating to 4.15 μmol Cu_3N reduced; over the entire 90 min, 8.13 C or 28.1 μmol equivalent of Cu_3N was passed. Given the layer thickness ($\sim$600 nm) and the geometric area of the electrode, only 1.8 μmol of Cu_3N was expected. These observations indicate that the pre-treatment was sufficient to convert the Cu_3N layer to metallic Cu. After electrochemical pre-treatment, cross-section imaging shows the uniform Cu_3N layer is converted into a highly porous interconnected network (Figure 3E and Figure S9). Both HR-TEM (Figure 3F) and the SAED pattern (Figure 3G) demonstrate that Cu_3N is converted back to metallic Cu during the pre-treatment. The SAED shows a cubic pattern with 0.18 nm d-spacing, corresponding to exposed Cu (200) square lattice. This finding is in good agreement with out-of-plane XRD (Figure 3J), which showed a strong diffraction peak centered at 50.8° corresponding to metallic Cu (200). The formation of (200)-oriented Cu after the electrochemical reduction can be attributed to the lower work function and higher surface energy of the (200) facet than those for the (111) facet, which can lead to a higher etching rate in this direction.[40, 41] Furthermore, the exposure of Cu (200) planes was reported to promote the evolution of C_2 products such as ethylene and suppress the formation of methane.[10, 11] Moreover, no nitrogen signal was

13

detected by EDS mapping (Figure 3H), selective area EDS (Figure 3I), or XPS (Figure S5), further supporting the complete transformation of Cu_3N into metallic Cu during the pre-treatment step. An oxygen signal was evident in the EDS spectrum of the reduced Cu_3N sample (Figure 3I), which is most likely related to sample transfer and air exposure of the sample.

The formation of the highly porous metallic Cu film during the pre-treatment electrochemical reduction of Cu_3N is the result of removal of nitrogen from the lattice. As discussed, the molar densities of Cu atoms in Cu_3N and Cu is 0.141 and 0.090 mol cm^{-3}, respectively. Densification of the Cu atoms by a factor of 1.6 through removal of nitrogen produces a highly porous structure, which we attribute to film strain-induced void formation. The electrochemical reduction done at room temperature may be responsible for maintaining a high degree of porosity in the layer during its transformation. Further roughening might be possible by lowering the temperature with an ice bath or in non-aqueous electrolytes but confirmation of this hypothesis will require further investigations. We also note that CuP_{10} would have a densification factor of 19.6 potentially providing access to even greater volume contraction and further roughening.
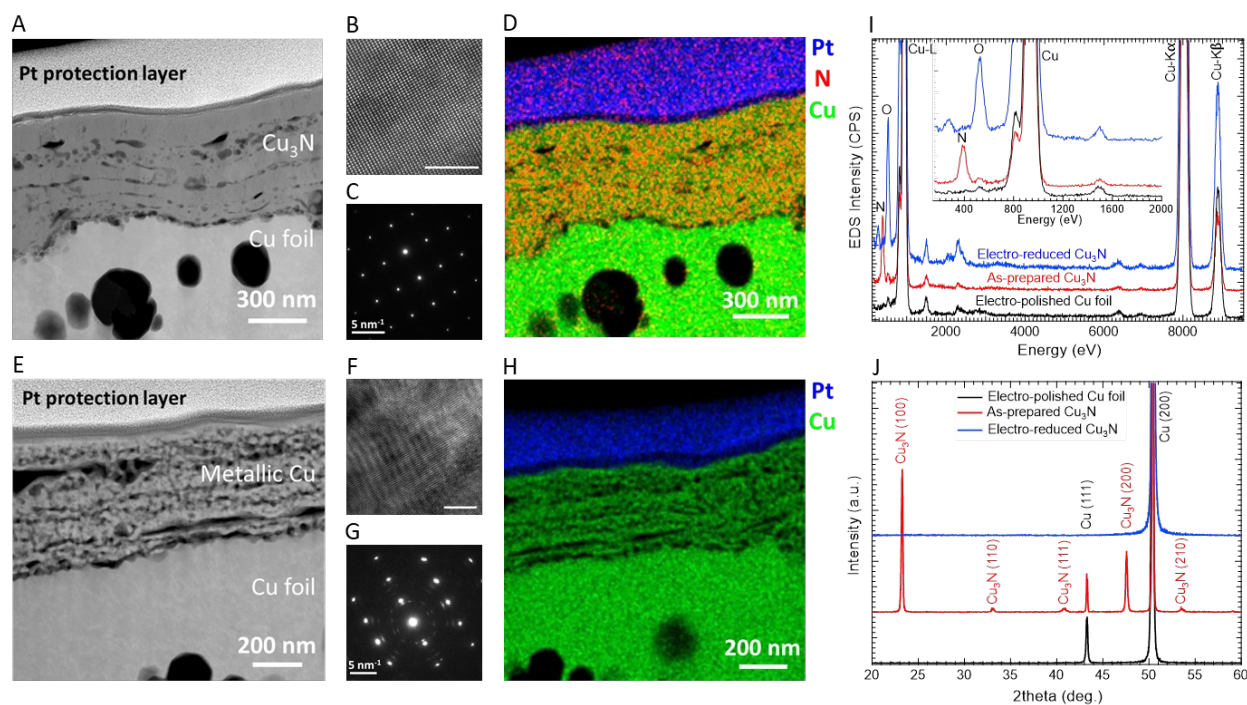
Figure 3. Microstructure and elemental composition of Cu₃N-derived Cu. (A) Cross-sectional HAADF-STEM view of the 30-min annealed Cu₃N layer. (B) Atomic-scale HR-TEM of the as-prepared Cu₃N layer (scale bar is 5 nm). (C) SAED pattern of the as-prepared Cu₃N layer. (D) STEM-EDS maps of as-prepared Cu₃N. (E) Cross-sectional HAADF-STEM view of the Cu₃N layer after 90 min electrochemical reduction. (F) Atomic-scale HR-TEM of the reduced Cu₃N layer (scale bar is 5 nm). (G) SAED pattern of the reduced Cu₃N layer. (H) STEM-EDS maps of the reduced Cu₃N layer. (I) Selective area EDS of the Cu₃N layer before and after the electrochemical reduction compared to the electrochemically polished Cu foil. (J) Out-of-plane XRD of the same samples shown in (I).

The CO_2 reduction activity of 30-min annealed Cu₃N-derived Cu was evaluated by chronoamperometric electrolysis in CO_2-saturated 0.1 M CsHCO₃ electrolyte.[42, 43] CsHCO₃ was selected because Cs^+ has the smallest hydrated cation radius compared to other alkali metal cations, which lead to a higher concentration of cations at the cathode and a larger surface charge density. This latter creates a stronger double layer field, which, in turn, enhances the adsorption of CO_2 and stabilizes the formation of *OCCO, an

intermediate in the formation of C_2 products.[44] Figure 4A shows the steady-state current densities averaged over 1-h electrolysis at each potential, with the H_2, C_1, C_2, and C_3 product distributions plotted in Figure 4B. A portion of missing FE observed at -0.6 V, probably arisen from the reduction current of Cu_xO formed during electrolyte switch after the pre-reduction step.[45, 46] The potential-dependence of each product is plotted in Figure 4C. The H_2 FE gradually decreases as the potential is reduced from -0.6 to -0.9 V vs. RHE, then increases slightly again when the potential reaches -1.0 V vs. RHE due to mass-transport limited current of dissolved CO_2.[43] Formate is another dominant product at low overpotentials. The FE for formate reaches a maximum FE of 35.2% at -0.7 V and then decreases with decreasing potential. Notably, no CH_4 was observed throughout the investigated potential region. The FE for CO, a vital intermediate for multi-carbon products, decreases monotonically from -0.6 V vs. RHE (FE = 21.3%) to -1.0 V vs. RHE (FE = 1.1%), whereas the FEs for C_2 (ethylene and ethanol) and C_3 products (allyl alcohol and n-propanol) increase correspondingly. C_2H_4 evolution starts at -0.7 V vs. RHE and the generation of oxygenates, involving >2e, starts at ~ -0.8 V, for which the overall C_{2+} FE gradually increases with decreasing applied potential. At -1.0V, this nitride-derived Cu electrode delivers a geometric current density of ~18.5 mA cm^{-2} (see also Figure S10 of partial current densities for each product at different applied potentials), reaching a maximum C_{2+} FE above 68% of which ~35% is due to oxygenates. Taking H_2 and C_2H_4 as representative CO_2RR products, we find that the FEs for these products remains stable with prolonged electrolysis (Figure S11). To the best of our knowledge, this is one of the most selective catalyst for producing multi-carbon products reported to date (Supporting Information, Table S1).[11, 24, 47-52]

We have recently proposed that the Cu surface roughness factor (RF) is a good descriptor for selectivity to multi-carbon product formed via the CO_2RR over Cu.[53] Higher surface roughness increases the exposure of under-coordinated Cu surface sites that strongly bind adsorbed CO, thereby

16

promoting the reduction of adsorbed CO rather than its desorption, and creating square sites next to steps that stabilize intermediates (e.g., OC-CO, OC-CHO) involved in the formation of C_2 products (C_2H_4 and C_2H_5OH).[21, 54]
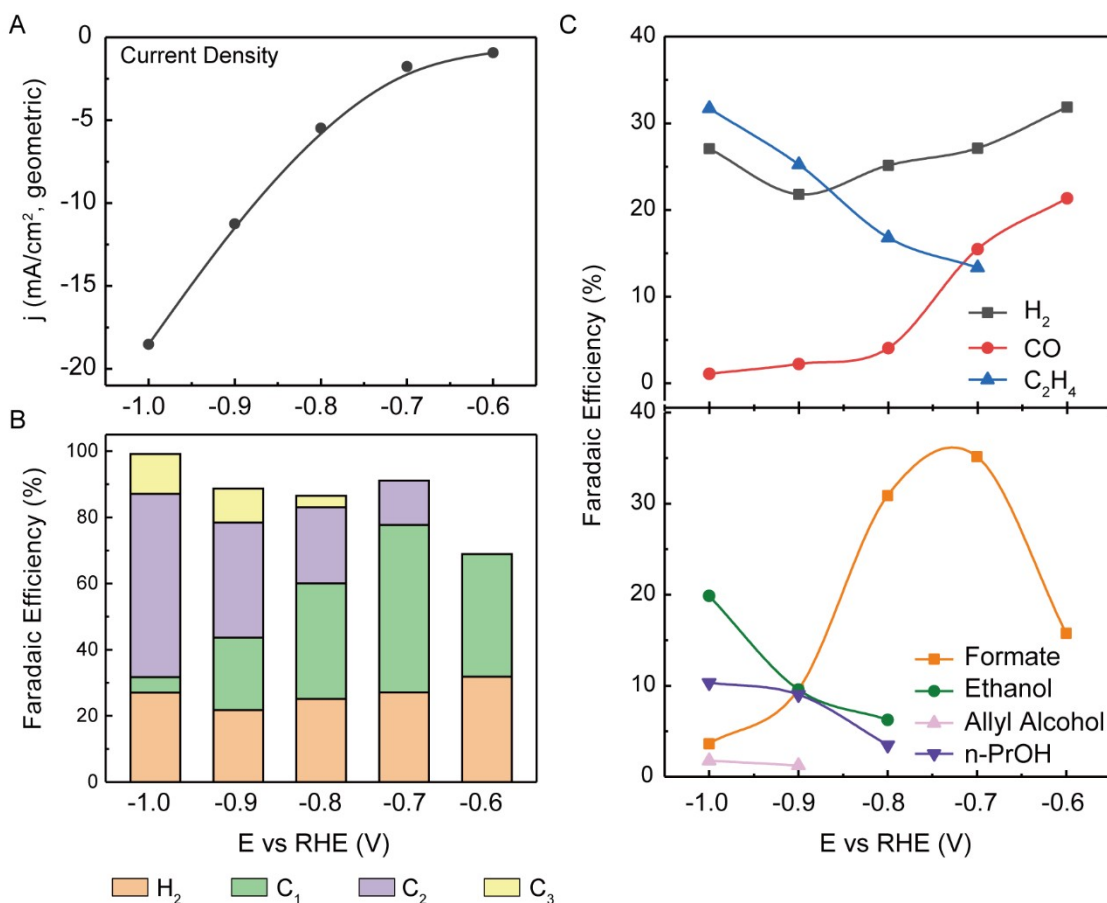

Figure 4. Electrocatalytic CO_2RR performance of electrochemical reduced Cu_3N catalyst within 0.1 M CO_2-saturated $CsHCO_3$ electrolyte. (A) steady-state current density averaged from 1-h electrolysis, together with potential-dependence of (B) Faradaic efficiencies for H_2, C_1, C_2, and C_3 products, and (C) detailed distribution of major CO_2RR products for a 30-min thermal annealed Cu_3N electrode (RF = 17.67).

The electrochemical surface area (ECSA), representative of the RF, of Cu_3N-derived Cu after 1-h CO_2RR electrolysis was determined by referencing to the double-layer capacitance of electro-polished Cu foil (RF = 1.00). The

surface RF of Cu_3N-derived Cu was altered by varying the thermal annealing time (see Figure S12). For 15-, 30-, and 60-min annealed samples the RF was 16.78, 17.67 and 19.78, respectively. The ratio of C_{2+}/C_1 products increased with increasing RF from 1.00 to 17.67 then leveled off to 19.78, as shown in Figure 5A. The CO_2 consumption rate is ca. ~ 30.45 nmol s^{-1} cm^{-2} on the most roughened Cu surface. This rate is close to the CO_2 mass transport limitation over a planar electrode in aqueous solution[43] suggesting a balance between RF and C_{2+} efficiency due to limitations of adsorbed CO availability for further C-C bond formation.

To compare the role of RF on the multi-carbon products selectivity in CO_2RR further, we examined roughened Cu foil electrodes produced by Ar^+ plasma bombardment for which the RF ranged from 1.42 to 3.64. Figure 5B shows the roughness dependence of the ratio of C_{2+} to overall CO_2 reduction products. Both Cu_3N-derived Cu catalysts and Ar^+ ion-roughened Cu foils follow a clear trend in RF; the C_{2+} selectivity increases with increasing Cu surface roughness independent of how the surfaces is roughened. This observation reinforces our earlier interpretation that controlled RF is of critical importance for improving CO_2RR efficiencies and selectivity. Increasing under-coordinated Cu sites improves multi-carbon product efficiency by binding adsorbed CO more strongly as compared to low-index Cu facets (e.g., Cu(111) and Cu(100)). Furthermore, an increased concentration of surface sites which having strong binding of CO also suppress the competitive adsorption of H (Figure S13), thus leading to an increased oxygenate/hydrocarbon ratio (Figure 5C). We also note that the high density of nanoscale-voids in the porous structure of the electrodes is expected to lead to an increase in the local pH at the electrode-electrolyte interface and, in turn, on the C_{2+}/C_1 selectivity. Hori *et al.* has reported that high local pH can largely suppress CH_4 generation.[19] We also note that the high density of nanoscale-voids in the electrode porous structure is expected to increase the local pH at the electrode-electrolyte interface and, in turn, suppressing methane generation with an increase on the C_{2+}/C_{1+} selectivity.
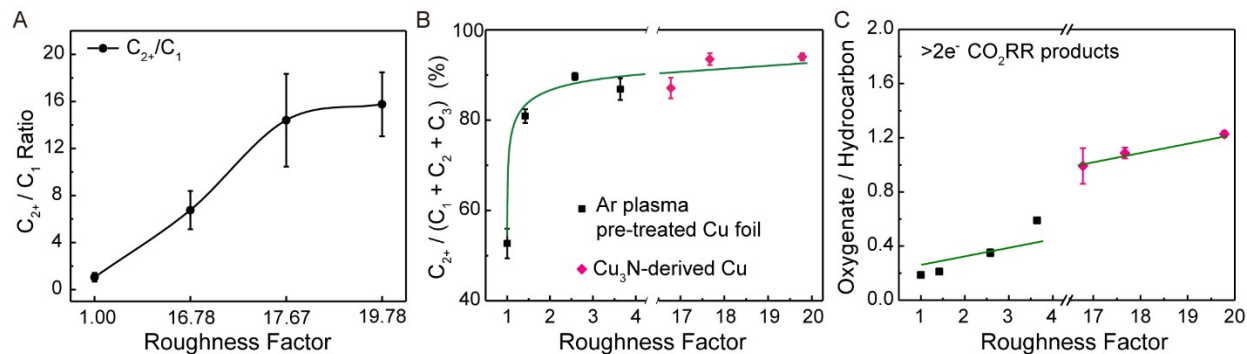
Figure 5. Surface Roughness dependence of CO_2RR products distribution. (A) Faradaic efficiency ratio of C_{2+} products versus C_1 products generated on Cu_3N-derived catalysts, with electro-polished Cu foil as reference (RF = 1.0), as a function of the surface roughness measured at a cathode potential of –1.0 V vs RHE. (B) C_{2+} products selectivity and (C) Faradaic efficiency ratio of oxygenate versus hydrocarbon products illustrated for physically roughened Cu foils obtained by Ar-plasma pretreatment and Cu_3N-derived Cu electrodes prepared with different annealing times; all measurements were made at a cathode potential of – 1 V vs RHE, within 0.1 M CO_2-saturated $CsHCO_3$.

CONCLUSIONS

In conclusion, we have developed an efficient Cu_3N-derived Cu catalyst that exhibits an exceptionally high Faradaic efficiency to C_{2+} products for CO_2 reduction in an aqueous solution of $CsHCO_3$ (0.1 M). The Cu_3N was formed by annealing a Cu-foil at temperatures as low as 400 °C in a mixture of NH_3/O_2. The active catalyst is produced by 90 min of electrochemical reduction of the Cu_3N covered Cu-foil in 0.1 M CO_2-saturated $CsHCO_3$ electrolyte. Analysis shows that all of the nitrogen in the as-prepared Cu_3N was eliminated leaving behind a mesoporous Cu structure that has ~ 17 times the roughness of the electro-polished Cu foil. The resulting Cu catalysts exhibits a Faradaic efficiency to C_{2+} products exceeding 68%, of which ~35% is C_{2+} oxygenates, when operated at a cathode potential of -1.0 V vs. RHE and a current density

of ~18.5 mA.cm^{-2}. The results of the present study extend those we reported recently for Cu roughened by Ar$^+$ bombardment in an Ar plasma and by oxidation in an O$_2$ plasma. In both cases, the Cu surface was roughened by up to a factor of four relative that of the starting electro-polished Cu surface. The performance of these catalysts demonstrated to be independent of the method of roughening and the active catalyst in all cases is metallic Cu. As illustrated in Fig. 5B, the ratio of C$_{2+}$/(C$_1$+C$_2$+C$_3$) products increases monotonically with increasing roughness.

REFERENCES

1. Mora, C.; Frazier, A. G.; Longman, R. J.; Dacks, R. S.; Walton, M. M.; Tong, E. J.; Sanchez, J. J.; Kaiser, L. R.; Stender, Y. O.; Anderson, J. M.; Ambrosino, C. M.; Fernandez-Silva, I.; Giuseffi, L. M.; Giambelluca, T. W., The projected timing of climate departure from recent variability. *Nature* **2013,** 502, 183.

2. Jacobson, T. A.; Kler, J. S.; Hernke, M. T.; Braun, R. K.; Meyer, K. C.; Funk, W. E., Direct human health risks of increased atmospheric carbon dioxide. *Nature Sustainability* **2019,** 2, 691.

3. Zhou, J.-H.; Zhang, Y.-W., Metal-based heterogeneous electrocatalysts for reduction of carbon dioxide and nitrogen: mechanisms, recent advances and perspective. *Reaction Chemistry & Engineering* **2018,** 3, (5), 591-625.

4. He, J.; Johnson, N. J. J.; Huang, A.; Berlinguette, C. P., Electrocatalytic Alloys for CO2 Reduction. *ChemSusChem* **2018,** 11, (1), 48-57.

5. Yamaguchi, A.; Yamamoto, M.; Takai, K.; Ishii, T.; Hashimoto, K.; Nakamura, R., Electrochemical CO2 Reduction by Ni-containing Iron Sulfides: How Is CO2 Electrochemically Reduced at Bisulfide-Bearing Deep-sea Hydrothermal Precipitates? *Electrochimica Acta* **2014,** 141, 311-318.

6. Chan, K.; Tsai, C.; Hansen, H. A.; Nørskov, J. K., Molybdenum Sulfides and Selenides as Possible Electrocatalysts for CO2 Reduction. *ChemCatChem* **2014,** 6, (7), 1899-1905.

7. Lum, Y.; Cheng, T.; Goddard, W. A.; Ager, J. W., Electrochemical CO Reduction Builds Solvent Water into Oxygenate Products. *Journal of the American Chemical Society* **2018,** 140, (30), 9337-9340.

8. Zheng, Y.; Vasileff, A.; Zhou, X.; Jiao, Y.; Jaroniec, M.; Qiao, S.-Z., Understanding the Roadmap for Electrochemical Reduction of CO2 to Multi-Carbon Oxygenates and Hydrocarbons on Copper-Based Catalysts. *Journal of the American Chemical Society* **2019,** 141, (19), 7646-7659.

9. Peterson, A. A.; Abild-Pedersen, F.; Studt, F.; Rossmeisl, J.; Nørskov, J. K., How copper catalyzes the electroreduction of carbon dioxide into hydrocarbon fuels. *Energy & Environmental Science* **2010,** 3, (9), 1311-1315.

10. Hori, Y.; Takahashi, I.; Koga, O.; Hoshi, N., Selective Formation of C2 Compounds from Electrochemical Reduction of CO2 at a Series of Copper Single Crystal Electrodes. *The Journal of Physical Chemistry B* **2002,** 106, (1), 15-17.

11. Jiang, K.; Sandberg, R. B.; Akey, A. J.; Liu, X.; Bell, D. C.; Nørskov, J. K.; Chan, K.; Wang, H., Metal ion cycling of Cu foil for selective C–C coupling in electrochemical CO2 reduction. *Nature Catalysis* **2018,** 1, (2), 111-119.

12. Huo, Y.; Peng, X.; Liu, X.; Li, H.; Luo, J., High Selectivity Toward C2H4 Production over Cu Particles Supported by Butterfly-Wing-Derived Carbon Frameworks. *ACS Applied Materials & Interfaces* **2018,** 10, (15), 12618-12625.

13. Shen, S.; Peng, X.; Song, L.; Qiu, Y.; Li, C.; Zhuo, L.; He, J.; Ren, J.; Liu, X.; Luo, J., AuCu Alloy Nanoparticle Embedded Cu Submicrocone Arrays for Selective Conversion of CO2 to Ethanol. *Small* **2019,** 15, (37), 1902229.

14. Luo, M.; Wang, Z.; Li, Y. C.; Li, J.; Li, F.; Lum, Y.; Nam, D.-H.; Chen, B.; Wicks, J.; Xu, A.; Zhuang, T.; Leow, W. R.; Wang, X.; Dinh, C.-T.; Wang, Y.;

Wang, Y.; Sinton, D.; Sargent, E. H., Hydroxide promotes carbon dioxide electroreduction to ethanol on copper via tuning of adsorbed hydrogen. *Nature Communications* **2019,** 10, (1), 5814.

15. Kas, R.; Kortlever, R.; Milbrat, A.; Koper, M. T. M.; Mul, G.; Baltrusaitis, J., Electrochemical CO2 reduction on Cu2O-derived copper nanoparticles: controlling the catalytic selectivity of hydrocarbons. *Physical Chemistry Chemical Physics* **2014,** 16, (24), 12194-12201.

16. Mi, Y.; Shen, S.; Peng, X.; Bao, H.; Liu, X.; Luo, J., Selective Electroreduction of CO2 to C2 Products over Cu3N-Derived Cu Nanowires. *ChemElectroChem* **2019,** 6, (9), 2393-2397.

17. Qin, B.; Wang, H.; Peng, F.; Yu, H.; Cao, Y., Effect of the surface roughness of copper substrate on three-dimensional tin electrode for electrochemical reduction of CO2 into HCOOH. *Journal of CO2 Utilization* **2017,** 21, 219-223.

18. Sen, S.; Liu, D.; Palmore, G. T. R., Electrochemical Reduction of CO2 at Copper Nanofoams. *ACS Catalysis* **2014,** 4, (9), 3091-3095.

19. Hori, Y.; Murata, A.; Takahashi, R., Formation of hydrocarbons in the electrochemical reduction of carbon dioxide at a copper electrode in aqueous solution. *Journal of the Chemical Society, Faraday Transactions 1: Physical Chemistry in Condensed Phases* **1989,** 85, (8), 2309-2326.

20. Verdaguer-Casadevall, A.; Li, C. W.; Johansson, T. P.; Scott, S. B.; McKeown, J. T.; Kumar, M.; Stephens, I. E. L.; Kanan, M. W.; Chorkendorff, I., Probing the Active Surface Sites for CO Reduction on Oxide-Derived Copper Electrocatalysts. *Journal of the American Chemical Society* **2015,** 137, (31), 9808-9811.

21. Huang, Y.; Chen, Y.; Cheng, T.; Wang, L.-W.; Goddard, W. A., Identification of the Selective Sites for Electrochemical Reduction of CO to C2+ Products on Copper Nanoparticles by Combining Reactive Force Fields, Density Functional Theory, and Machine Learning. *ACS Energy Letters* **2018,** 3, (12), 2983-2988.

22. Resasco, J.; Chen, L. D.; Clark, E.; Tsai, C.; Hahn, C.; Jaramillo, T. F.; Chan, K.; Bell, A. T., Promoter Effects of Alkali Metal Cations on the Electrochemical Reduction of Carbon Dioxide. *Journal of the American Chemical Society* **2017,** 139, (32), 11277-11287.

23. Veenstra, F. L. P.; Martín, A. J.; Pérez-Ramírez, J., Nitride-Derived Copper Modified with Indium as a Selective and Highly Stable Catalyst for the Electroreduction of Carbon Dioxide. *ChemSusChem* **2019,** 12, (15), 3501-3508.

24. Liang, Z.-Q.; Zhuang, T.-T.; Seifitokaldani, A.; Li, J.; Huang, C.-W.; Tan, C.-S.; Li, Y.; De Luna, P.; Dinh, C. T.; Hu, Y.; Xiao, Q.; Hsieh, P.-L.; Wang, Y.; Li, F.; Quintero-Bermudez, R.; Zhou, Y.; Chen, P.; Pang, Y.; Lo, S.-C.; Chen, L.-J.; Tan, H.; Xu, Z.; Zhao, S.; Sinton, D.; Sargent, E. H., Copper-on-nitride enhances the stable electrosynthesis of multi-carbon products from CO2. *Nature Communications* **2018,** 9, (1), 3828.

25. Yin, Z.; Yu, C.; Zhao, Z.; Guo, X.; Shen, M.; Li, N.; Muzzio, M.; Li, J.; Liu, H.; Lin, H.; Yin, J.; Lu, G.; Su, D.; Sun, S., Cu3N Nanocubes for Selective Electrochemical Reduction of CO2 to Ethylene. *Nano Letters* **2019,** 19, (12), 8658.

26. Matsuzaki, K.; Harada, K.; Kumagai, Y.; Koshiya, S.; Kimoto, K.; Ueda, S.; Sasase, M.; Maeda, A.; Susaki, T.; Kitano, M.; Oba, F.; Hosono, H., High-

Mobility p-Type and n-Type Copper Nitride Semiconductors by Direct Nitriding Synthesis and In Silico Doping Design. *Advanced Materials* **2018,** 30, (31), 1801968.

27.   Nakamura, S.; Harada, Y.; Seno, M., Novel metalorganic chemical vapor deposition system for GaN growth. *Applied Physics Letters* **1991,** 58, (18), 2021-2023.

28.   Ukropec, R.; Kuster, B. F. M.; Schouten, J. C.; van Santen, R. A., Low temperature oxidation of ammonia to nitrogen in liquid phase. *Applied Catalysis B: Environmental* **1999,** 23, (1), 45-57.

29.   Il'chenko, N. I., Catalytic Oxidation of Ammonia. *Russian Chemical Reviews* **1976,** 45, (12), 1119-1134.

30.   Hahn, T. A., Thermal Expansion of Copper from 20 to 800 K—Standard Reference Material 736. *Journal of Applied Physics* **1970,** 41, (13), 5096-5101.

31.   von Fieandt, L.; Larsson, T.; Lindahl, E.; Bäcke, O.; Boman, M., Chemical vapor deposition of TiN on transition metal substrates. *Surface and Coatings Technology* **2018,** 334, 373-383.

32.   Kuzmin, A.; Anspoks, A.; Kalinko, A.; Timoshenko, J.; Nataf, L.; Baudelet, F.; Irifune, T., Origin of Pressure-Induced Metallization in Cu3N: An X-ray Absorption Spectroscopy Study. *physica status solidi (b)* **2018,** 255, (11), 1800073.

33.   An, B.; Li, Z.; Song, Y.; Zhang, J.; Zeng, L.; Wang, C.; Lin, W., Cooperative copper centres in a metal–organic framework for selective conversion of CO2 to ethanol. *Nature Catalysis* **2019,** 2, 709.

34.   Ikuno, T.; Zheng, J.; Vjunov, A.; Sanchez-Sanchez, M.; Ortuño, M. A.; Pahls, D. R.; Fulton, J. L.; Camaioni, D. M.; Li, Z.; Ray, D.; Mehdi, B. L.; Browning, N. D.; Farha, O. K.; Hupp, J. T.; Cramer, C. J.; Gagliardi, L.; Lercher, J. A., Methane Oxidation to Methanol Catalyzed by Cu-Oxo Clusters Stabilized in NU-1000 Metal–Organic Framework. *Journal of the American Chemical Society* **2017,** 139, (30), 10294-10301.

35.   Timoshenko, J.; Anspoks, A.; Kalinko, A.; Kuzmin, A., Local structure of copper nitride revealed by EXAFS spectroscopy and a reverse Monte Carlo/evolutionary algorithm approach. *Physica Scripta* **2016,** 91, (5), 054003.

36.   Bocharov, D.; Anspoks, A.; Timoshenko, J.; Kalinko, A.; Krack, M.; Kuzmin, A., Interpretation of the Cu K-edge EXAFS spectra of Cu3N using ab initio molecular dynamics. *Radiation Physics and Chemistry* **2018,** 23, 108100.

37.   Timoshenko, J.; Anspoks, A.; Kalinko, A.; Kuzmin, A., Thermal disorder and correlation effects in anti-perovskite-type copper nitride. *Acta Materialia* **2017,** 129, 61-71.

38.   Konishi, S.; Moriyama, M.; Murakami, M., Effect of Annealing Atmosphere on Void Formation in Copper Interconnects. *MATERIALS TRANSACTIONS* **2002,** 43, (7), 1624-1628.

39.   Yao, B.; Sun, T.; Kumar, V.; Barmak, K.; Coffey, K. R., Grain growth and void formation in dielectric-encapsulated Cu thin films. *Journal of Materials Research* **2008,** 23, (7), 2033-2039.

40.   Wang, Z.; Yang, G.; Zhang, Z.; Jin, M.; Yin, Y., Selectivity on Etching: Creation of High-Energy Facets on Copper Nanocrystals for CO2 Electrochemical Reduction. *ACS Nano* **2016,** 10, (4), 4559-4564.

41. Skriver, H. L.; Rosengaard, N. M., Surface energy and work function of elemental metals. *Physical Review B* **1992,** 46, (11), 7157-7168.

42. Singh, M. R.; Kwon, Y.; Lum, Y.; Ager, J. W.; Bell, A. T., Hydrolysis of Electrolyte Cations Enhances the Electrochemical Reduction of CO2 over Ag and Cu. *Journal of the American Chemical Society* **2016,** 138, (39), 13006-13012.

43. Clark, E. L.; Resasco, J.; Landers, A.; Lin, J.; Chung, L.-T.; Walton, A.; Hahn, C.; Jaramillo, T. F.; Bell, A. T., Standards and Protocols for Data Acquisition and Reporting for Studies of the Electrochemical Reduction of Carbon Dioxide. *ACS Catalysis* **2018,** 8, (7), 6560-6570.

44. Ringe, S.; Clark, E. L.; Resasco, J.; Walton, A.; Seger, B.; Bell, A. T.; Chan, K., Understanding cation effects in electrochemical CO2 reduction. *Energy & Environmental Science* **2019,** 12, (10), 3001-3014.

45. Farmand, M.; Landers, A. T.; Lin, J. C.; Feaster, J. T.; Beeman, J. W.; Ye, Y.; Clark, E. L.; Higgins, D.; Yano, J.; Davis, R. C.; Mehta, A.; Jaramillo, T. F.; Hahn, C.; Drisdell, W. S., Electrochemical flow cell enabling operando probing of electrocatalyst surfaces by X-ray spectroscopy and diffraction. *Physical Chemistry Chemical Physics* **2019,** 21, (10), 5402-5408.

46. Scott, S. B.; Hogg, T. V.; Landers, A. T.; Maagaard, T.; Bertheussen, E.; Lin, J. C.; Davis, R. C.; Beeman, J. W.; Higgins, D.; Drisdell, W. S.; Hahn, C.; Mehta, A.; Seger, B.; Jaramillo, T. F.; Chorkendorff, I., Absence of Oxidized Phases in Cu under CO Reduction Conditions. *ACS Energy Letters* **2019,** 4, (3), 803-804.

47. Hahn, C.; Hatsukade, T.; Kim, Y.-G.; Vailionis, A.; Baricuatro, J. H.; Higgins, D. C.; Nitopi, S. A.; Soriaga, M. P.; Jaramillo, T. F., Engineering Cu surfaces for the electrocatalytic conversion of CO2: Controlling selectivity toward oxygenates and hydrocarbons. *Proceedings of the National Academy of Sciences* **2017,** 114, (23), 5918.

48. Dutta, A.; Rahaman, M.; Luedi, N. C.; Mohos, M.; Broekmann, P., Morphology Matters: Tuning the Product Distribution of CO2 Electroreduction on Oxide-Derived Cu Foam Catalysts. *ACS Catalysis* **2016,** 6, (6), 3804-3814.

49. Ren, D.; Deng, Y.; Handoko, A. D.; Chen, C. S.; Malkhandi, S.; Yeo, B. S., Selective Electrochemical Reduction of Carbon Dioxide to Ethylene and Ethanol on Copper(I) Oxide Catalysts. *ACS Catalysis* **2015,** 5, (5), 2814-2821.

50. Zhuang, T.-T.; Liang, Z.-Q.; Seifitokaldani, A.; Li, Y.; De Luna, P.; Burdyny, T.; Che, F.; Meng, F.; Min, Y.; Quintero-Bermudez, R.; Dinh, C. T.; Pang, Y.; Zhong, M.; Zhang, B.; Li, J.; Chen, P.-N.; Zheng, X.-L.; Liang, H.; Ge, W.-N.; Ye, B.-J.; Sinton, D.; Yu, S.-H.; Sargent, E. H., Steering post-C–C coupling selectivity enables high efficiency electroreduction of carbon dioxide to multi-carbon alcohols. *Nature Catalysis* **2018,** 1, (6), 421-428.

51. Mistry, H.; Varela, A. S.; Bonifacio, C. S.; Zegkinoglou, I.; Sinev, I.; Choi, Y.-W.; Kisslinger, K.; Stach, E. A.; Yang, J. C.; Strasser, P.; Cuenya, B. R., Highly selective plasma-activated copper catalysts for carbon dioxide reduction to ethylene. *Nature Communications* **2016,** 7, (1), 12123.

52. Gao, D.; McCrum, I. T.; Deo, S.; Choi, Y.-W.; Scholten, F.; Wan, W.; Chen, J. G.; Janik, M. J.; Roldan Cuenya, B., Activity and Selectivity Control in CO2 Electroreduction to Multicarbon Products over CuOx Catalysts via Electrolyte Design. *ACS Catalysis* **2018,** 8, (11), 10012-10020.

24

53. Jiang, K.; Ebaid, M.; Huang, Y.; Cooper, J. K.; Bell, A. T., 17th International Congress On Catalysis, San Diego, CA, USA, 14-19 June 2020.

54. Birdja, Y. Y.; Pérez-Gallent, E.; Figueiredo, M. C.; Göttle, A. J.; Calle-Vallejo, F.; Koper, M. T. M., Advances and challenges in understanding the electrocatalytic conversion of carbon dioxide to fuels. *Nature Energy* **2019,** 4, (9), 732-745.

Table of Contents (TOC)
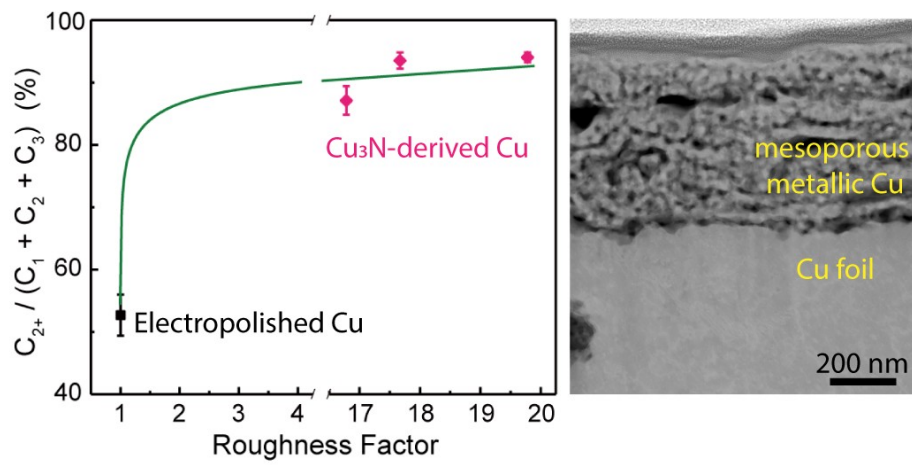
Supporting Information:

Surface morphology as a function of annealing time, XRD analysis, XAS, XPS, FIB/SEM, TEM/EDS, CA of the electrochemical reduction of Cu_3N into metallic Cu, HR-TEM of Cu_3N before and after the electrochemical reduction, partial current densities of C-products, CO_2 reduction stability, ECSA on Cu_3N samples with varied annealing time, surface roughness impact on the H_2 Faradaic efficiency, and CO_2RR performance summary